Carbon 179 (2021) 327–336

Contents lists available at ScienceDirect

Carbon

journal homepage: www.elsevier.com/locate/carbon

Research Article

Ultra-small Fe_3O_4 nanoparticles encapsulated in hollow porous carbon nanocapsules for high performance supercapacitors

Lijian Wang [a], Fenghua Liu [b, c, d], Avishek Pal [a], Yuesheng Ning [a], Zan Wang [b, c, d], Binyuan Zhao [a, **], Robert Bradley [e, f, g], Weiping Wu [b, c, d, *]

[a] State Key Laboratory of Metal Matrix Composites, School of Materials Science and Engineering, Shanghai Jiao Tong University, Shanghai, 200240, China
[b] State Key Laboratory of High Field Laser Physics, Shanghai Institute of Optics and Fine Mechanics, Chinese Academy of Sciences, Shanghai, 201800, China
[c] Key Laboratory of Materials for High Power Laser, Shanghai Institute of Optics and Fine Mechanics, Chinese Academy of Sciences, Shanghai, 201800, China
[d] Laboratory of Thin Film Optics, Shanghai Institute of Optics and Fine Mechanics, Chinese Academy of Sciences, Shanghai, 201800, China
[e] Department of Materials, University of Oxford, 16 Parks Road, Oxford, OX1 3PH, United Kingdom
[f] MatSurf Ltd, The Old Stables Marion Lodge, Little Salkeld, Penrith, Cumbria, CA10 1NW, United Kingdom
[g] School of Energy Resources, University of Wyoming, Laramie, WY, 82071, USA

ARTICLE INFO

Article history:
Received 16 January 2021
Received in revised form
19 March 2021
Accepted 3 April 2021
Available online 13 April 2021

Keywords:
Supercapacitors
Porous carbon nanocapsules
Incipient wetness impregnation
Gravimetric capacitance
Volumetric capacitance

ABSTRACT

A new nanoscale architecture of Fe_3O_4-carbon hybrid materials was developed by a vacuum incipient wetness procedure. The amount of Fe_3O_4 nanoparticles were controllably confined inside the cavity of the bowl-shaped hollow porous carbon nanocapsules (CNB). TEM images and TG curves proved that different loading of Fe_3O_4 small nanoparticles (NPs) with a diameter less than 50 nm were stored in CNB. Benefiting from the synergistic effect of the appropriate amount of uniformly dispersed Fe_3O_4 NPs and bowl-shaped carbon nano-capsules with high specific surface area, high conductivity and high amount of Nitrogen (N) and oxygen (O) elemental doping of Fe_3O_4@CNB, the new architecture provides good reversibility for the transport of electrolyte ions. When tested in supercapacitor devices, Fe_3O_4@CNB-2 (containing 40.3 wt% Fe_3O_4) exhibited the highest gravimetric (466 F g^{-1}) and volumetric capacitance (624 F cm^{-3}). The supercapacitors based on these materials also showed excellent cycling stability (92.4% capacitance retention after 5000 cycles). This class of Fe_3O_4-carbon hybrid materials has excellent electrochemical properties, and its synthesis strategy can be extended to construct other hybrid materials for various applications, such as biomedicine, catalysis, energy harvest, energy storage and so on.

1. Introduction

Supercapacitors have become one of the desirable energy storage devices due to their versatility and energy efficiency for fast energy storage and transmission [1–3]. Due to their outstanding characteristics such as high-power density, fast charge/discharge capabilities, broad operating temperature range, environmental friendliness and excellent long service life, they have been widely utilized in different fields, such as digital communication equipment, backup power systems, hybrid vehicles, and portable electronics [4,5].

There are two different types of mechanism for energy storage in the supercapacitor devices, including double layer capacitance (EDLCs) and Faradaic pseudocapacitance (PC). EDLCs can maintain good electron or ion alignment in the interface of carbon electrode and electrolyte which allows the accumulation of electric charges on the electrode/electrolyte accessible surface. Carbon based materials such as porous carbon [6,7], carbon nanofiber [8], carbon nanotubes [9], and graphene [10–12], are mostly used as EDLCs electrode materials because they have a high specific surface area, superior electrical conductivity and low cost. However, the limited specific capacitance of EDLCs has limited its usage in practical power applications [13]. Faradaic pseudocapacitance, generating capacitance by fast and reversible oxidation-reduction reactions or chemical adsorption/desorption reaction via surface and near-surface, exhibiting much higher capacitance value than that of EDLCs. However, pseudocapacitance electrode material has poor electronic and ionic conductivities, resulting in unsatisfactory rate

* Corresponding author. State Key Laboratory of High Field Laser Physics, Shanghai Institute of Optics and Fine Mechanics, Chinese Academy of Sciences, Shanghai, 201800, China.
** Corresponding author.
E-mail addresses: byzhao@sjtu.edu.cn (B. Zhao), wuwp@siom.ac.cn (W. Wu).

https://doi.org/10.1016/j.carbon.2021.04.024
0008-6223/

capability and reversibility [14]. Therefore, to achieve higher overall electrochemical performance, it is necessary to design composite materials that combine these two mechanisms of charge storage [15].

In the case of pseudocapacitive electrode material, Fe_3O_4 is one of the cost-effective and environmental friendly materials [16,17], which shows a high specific capacitance because of its oxidation states and susceptibility to reversible redox Faraday reactions in the aqueous solution [18]. Specifically, Vijayamohanan et al. [19] investigated the Faraday reaction mechanism of Fe_3O_4 in aqueous solution based on the following equation: $Fe_3O_4 + 2e^- + 4H_2O \rightarrow 3Fe(OH)_2 + 2OH^-$. However, due to their low specific surface area and porosity, the trend to aggregate together, poor electrical conductivity and sluggish ionic diffusion during the charge/discharge process, pure Fe_3O_4 nanoparticles as an electrode material for supercapacitors have an unsatisfactory specific capacitance, high interfacial resistance, poor rate performance, and degraded cycle life in aqueous electrolyte [20]. To solve this, one of the most effective methods is to composite Fe_3O_4 nanoparticles with carbon material with a higher specific surface area and better conductivity [21]. Particularly, hollow carbon nanocapsules [22], as a new type of nanostructure, due to their large specific surface area, low density, large internal space, thin shell thickness, as well as high electrical conductivity, have broad application prospects. The hollow porous structure enhances the electrolyte diffusion/ion transport and the internal hollow structure can be used to load oxide nanoparticles, which greatly inhibits their degradation during electrochemical processes [23]. However, in most research, the poorly conductive Fe_3O_4 nanoparticles are often loaded on the outer surface of the carbon sphere, which may block the pores of the carbon sphere, reducing both the ionic and electric conductivities [24]. Moreover, the direct exposure of Fe_3O_4 to the electrolyte made it less stable during long periods of cycling at high current densities, resulting in an insufficient enhancement for electrochemical performance [25,26]. Therefore, it is essential to construct an optimized structure to fully utilize the synergistic effect between the carbon and Fe_3O_4 nanoparticles for supercapacitors.

Herein, a new nanoscale architecture of encapsulated Fe_3O_4 nanoparticles with bowl-shaped carbon nanocapsules was prepared by a facile method. The amount of Fe_3O_4 nanoparticles were controllably confined inside the cavity of the hollow porous bowl-shaped carbon nanocapsules (CNB) by a vacuum incipient wetness procedure. The bowl-shaped CNB with high conductivity can provide a smaller void volume, which could be filled with the appropriate amount of Fe_3O_4 nanoparticles. It overcomes the deficiency of lower electrical conductivity and lower effective utilization of Fe_3O_4 nanoparticles caused by the agglomeration and stacking. The combination of the synergistic effect of Fe_3O_4 NPs, the bowl-shaped geometry of CNB, the high specific surface area, the high concentration nitrogen (N) and oxygen (O) elemental doping enables outstanding gravimetric capacitance and volumetric capacitance, excellent capacitance retention and high cycling stability of the obtained Fe_3O_4@CNB.

2. Experimental section

2.1. Synthesis of CNB with bowl-shaped structure

CNB with a bowl-shaped structure was synthesized by a facile method according to our previous work [27]. Typically, 0.5g SiO_2 spheres with an average diameter of 190 ± 10 nm as a hard template, were dispersed in 100 ml pre-mixed ethanol and water solution (water: ethanol = 7:3). Then, m-dihydroxybenzene (resorcinol), formaldehyde, ethylenediamine and TEOS were added in sequence under magnetic stirring at 35 °C for 24 h. After the reaction, the suspension was centrifuged at 7000 rpm. The as-prepared samples were then washed with DI water and dried at 60 °C. Then they were carbonized at 900 °C for 2 h under Argon (Ar). The obtained samples were denoted as SiO_2@C/SiO_2. Both the enclosed silica and the silica entwined with carbon shells were then removed by etching Silica@carbon spheresthe SiO_2@C/SiO_2 with 10% hydrofluoric acid (HF). The hollow porous spherical carbon shells were deflated and the CNBs with bowl-shaped structures were obtained.

2.2. Synthesis of Fe_3O_4@CNB

Fe_3O_4@CNBcomposites were synthesized by the vacuum incipient wetness impregnation method. Firstly, the CNBs were sealed in a vessel and degassed at 80 °C for 1 h. Then, under vacuum, an ethanol solution of 2 mol L^{-1} ferric nitrate was added dropwise on the CNB until reaching the incipient wetness impregnation. Finally, Fe_3O_4@CNB was obtained by sintering under a nitrogen atmosphere at 350 °C for 2 h. For comparison, wet-impregnated samples were also dried and then repeatedly wet-impregnated to obtain Fe_3O_4@CNB composites with different Fe_3O_4 loadings. The samples obtained by incipient wetness impregnations one, three and five times are marked as Fe_3O_4@CNB-1, Fe_3O_4@CNB-2, and Fe_3O_4@CNB-3, respectively.

2.3. Materials characterization

The obtained samples were characterized by the Scanning Electron Microscopy SEM (TESCAN Mira3) and Transmission Electron Microscopy TEM (JEOL JEM-2100F). The X-ray diffraction XRD patterns were collected on a Bruker D8 Advance Da Vinci operated with Cu $K\alpha$ radiation at 40 kV and 30 mA. The X-ray photoelectron spectroscopy XPS tests were performed on a Kratos AXIS Ultra DLD using monochromatic Al $K\alpha$ X-ray source. The Raman spectra were carried out using a Horiba Jobin Yvon HR 800 Raman spectrometer. The thermo-gravimetric analysis (TGA) was investigated by a NETZSCH STA 449F3 thermo-gravimetric analyzer at a heating rate of 10 °C min^{-1} in the air. The Brunauer-Emmet-Teller (BET) adsorption-desorption isotherms were tested on a TriStar 3000 analyzer at 77 K and the pore size distributions were calculated by the Nonlocal density functional theory (NLDFT) model. The magnetic measurements were carried out on a Magnetic Property Measurement System (Quantum Design MPMS3).

2.4. Electrochemical measurements

The electrochemical performances of materials were tested with a three-electrode configuration in the 6 M KOH electrolyte using a CHI660E electrochemical workstation (Shanghai, China). Typically, approximately 2.0 mg of active material was mixed with acetylene black and PTFE (polytetrafluoroethylene) to form a homogeneous slurry (80 wt% active material, 10 wt% acetylene black and10 wt% PTFE) and coated on nickel foam (1 × 1 cm), and then dried at 100 °C for 12 h to obtain the working electrode. A piece of platinum and a Hg/HgO electrode were used as counter and reference electrodes, respectively. The scan rates of the cyclovoltammetry (CV) were from 5 to 200 mV s^{-1} under a potential window from 0 V to 1 V, and the current densities of Galvanic charge-discharge (GCD) varied from 0.2 to 10 A g^{-1}. Electrochemical impedance spectroscopy (EIS) was measured in a frequency range from 10^{-1}–10^5 Hz.

3. Results and discussion

The synthesis procedure of the Fe_3O_4-carbon hybrid materials is illustrated in Scheme 1. Firstly, the bowl-shaped hollow carbon

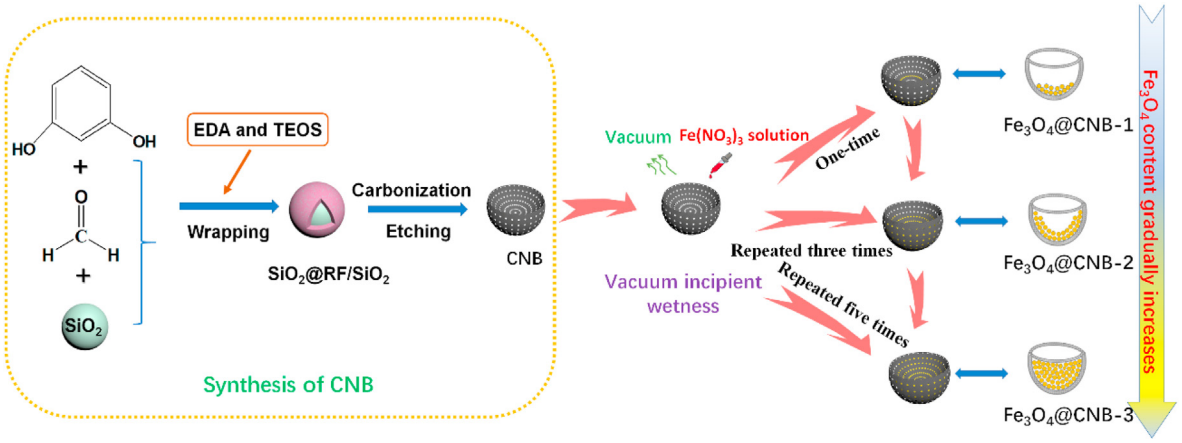

Scheme 1. Schematic synthesis processes of Fe_3O_4@CNBs by vacuum incipient wetness. (EDA: ethylenediamine; TEOS: tetraethoxysilane; CNB: carbon nanobowl).

nanocapsules prepared by our previous method [27] were used as growth reactors for Fe_3O_4 nanoparticles. By using different ratios of the carbon precursor and the porogenic agent tetraethyl orthosilicate (TEOS), the geometry of the carbon nanocapsules can be obtained, from the hollow sphere, to the spherical crown, and to the bowl shape. In detail, with Ethylenediamine (EDA) as the catalyst, a layer of m-dihydroxybenzene (resorcinol)-formaldehyde containing a small amount of fine SiO_2 nanoparticles was formed around the surface of silica (SiO_2) spheres (diameter 190 ± 10 nm), which were carbonized to obtain SiO_2@C intermediate product doped with SiO_2 small particles. Subsequently, the SiO_2 spheres and the smaller SiO_2 NPs doped in the carbon shell were simultaneously removed by etching. The thin porous spherical carbon shell cannot self-support the spherical structure during the etching of the inner SiO_2 spherical template, and gradually collapses inward like a deflated ball to form a bowl-like structure [28]. CNB with bowl shape was then produced after all SiO_2 had been removed. Notably, the prepared CNB materials with bowl-shaped structures have a high specific surface area, high concentrations of nitrogen (N) and oxygen (O) elemental doping.

Then, $Fe(NO_3)_3 \cdot 9H_2O$ in ethanol solution, as the precursor of Fe_3O_4, was absorbed by the CNB. The absorption process was achieved completely by the vacuum incipient wetness method. The CNB with semi-concaves could act as a nanoreactor. Pure CNB with a hollow internal cavity structure has a high specific surface area, indicating that the driving force behind the filling of the hollow core of the carbon capsules by the inorganic compound solution is the capillary motion through the mesopores of the carbon shell during vacuum incipient wetness process. Then, the surface of CNB was rinsed by rapid suction filtration of ethanol to remove the $Fe(NO_3)_3 \cdot 9H_2O$ precursor remaining on the surface of CNB. This ensures that Fe_3O_4 will not grow on the outer surface of the CNB. After evaporation of the ethanol solvent and subsequent thermal treatment, Fe_3O_4@CNB was prepared. For comparison, Fe_3O_4-carbon hybrid materials with different Fe_3O_4 contents were obtained by repeated vacuum initial wet impregnation of $Fe(NO_3)_3 \cdot 9H_2O$ ethanol solution, and the samples were labeled as Fe_3O_4@CNB-1 (one-time vacuum incipient wetness), Fe_3O_4@CNB-2 (incipient wetness impregnation repeated three times), and Fe_3O_4@CNB-3 (incipient wetness impregnation repeated five times). The unique structure of the Fe_3O_4-carbon hybrid materials can provide a conductive shell with a stable structure for different contents of Fe_3O_4 nanoparticles, thereby enhancing charge transfer and improving the capacitance performance.

The geometry and the surface morphology and microstructure of the as-prepared CNB and Fe_3O_4@CNB samples were characterized by SEM and TEM. As shown in Fig. 1a–d, both CNB and Fe_3O_4@CNB have similar uniform bowl-shaped structure with a 200 nm (±10 nm) diameter on average, and all Fe_3O_4@CNB samples have smooth surface with only a tiny amounts of impurities, indicating that $Fe(NO_3)_3 \cdot 9H_2O$ was perfectly impregnated into the hollow interior of CNB by the vacuum incipient wetness method. When the number of impregnation times of $Fe(NO_3)_3 \cdot 9H_2O$ solution was repeated more than five times, as shown in Fig. S1, some small Fe_3O_4 particles are attached to the outer surface of CNB, which may not be conducive to enhancing the conductivity and chemical stability of the sample. TEM images (Fig. 1e–h) revealed that CNB has a uniform bowl-shaped structure.

The thickness of the carbon shell is about 8 nm and Fe_3O_4 nanoparticles with a size less than 50 nm are uniformly distributed in the hollow interior of CNB. Clearly, Fe_3O_4@CNB samples with different Fe_3O_4 loadings can be obtained by controlling the repeated impregnation times. Only a small amount of Fe_3O_4 nanoparticles is located at the bottom of the cavities in Fe_3O_4@CNB-1, while more than half of the hollow interior is filled with Fe_3O_4 nanoparticles in Fe_3O_4@CNB-2, and the cavities are nearly filled with Fe_3O_4 nanoparticles in Fe_3O_4@CNB-3. As shown by the low magnification TEM (Fig. S2), the small Fe_3O_4 nanoparticles tend to agglomerate inside the CNB in the hollow interior of CNB, which may result from the shrinkage of the inorganic components in the precursors during heating. The Energy-Dispersive Spectroscopy (EDS) mapping analysis (Fig. S3) also proves that all Fe is concentrated in the internal of the hollow interior of the Fe_3O_4@CNB-2, indicating that nanoscale architecture of Fe_3O_4-carbon hybrid materials can be obtained by vacuum incipient wetness impregnation method.

Thermogravimetric analysis (TGA) was performed to evaluate the thermal stability and to figure out the Fe_3O_4 content of the Fe_3O_4-carbon hybrid materials. As shown in Fig. 2a, the weight retentions of pure CNB, Fe_3O_4@CNB-1, Fe_3O_4@CNB-2, and Fe_3O_4@CNB-3 after high temperature calcination are 2.6%, 33.3%, 45.7% and 67.7%, respectively. The low weight retention of pure CNB confirms its high purity. During the calcination in the air atmosphere, all the Fe_3O_4 is oxidized to form Fe_2O_3, and the carbon in the composite product is correspondingly oxidized to carbon dioxide [29]. According to these two conversion reactions, the contents of Fe_3O_4 in the four samples were roughly estimated to be 0, 22.5%, 36.6% and 57.4%, respectively. The Fe_3O_4 content increased gradually, which was consistent with the TEM results.

The crystallinity of the samples was examined by powder X-ray

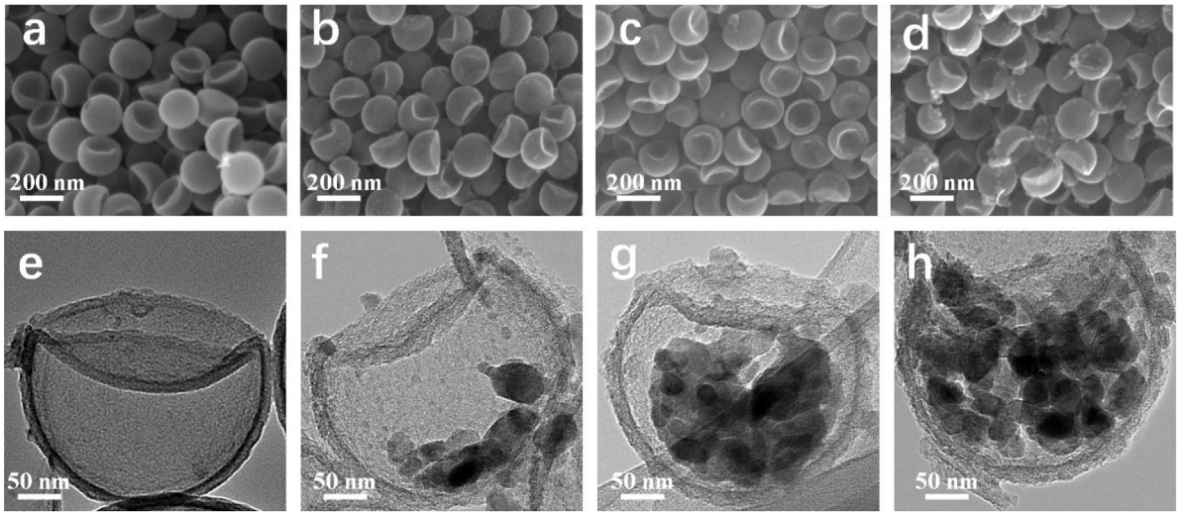

Fig. 1. Scanning Electron Microscope (SEM) images of Fe_3O_4-carbon hybrid materials with different Fe_3O_4 contents, (a) CNB, (b) Fe_3O_4@CNB-1, (c) Fe_3O_4@CNB-2, and (d) Fe_3O_4@CNB-3; Transmission Electron Microscopy (TEM) images of (e) CNB, (f) Fe_3O_4@CNB-1, (g) Fe_3O_4@CNB-2, and (h) Fe_3O_4@CNB-3.

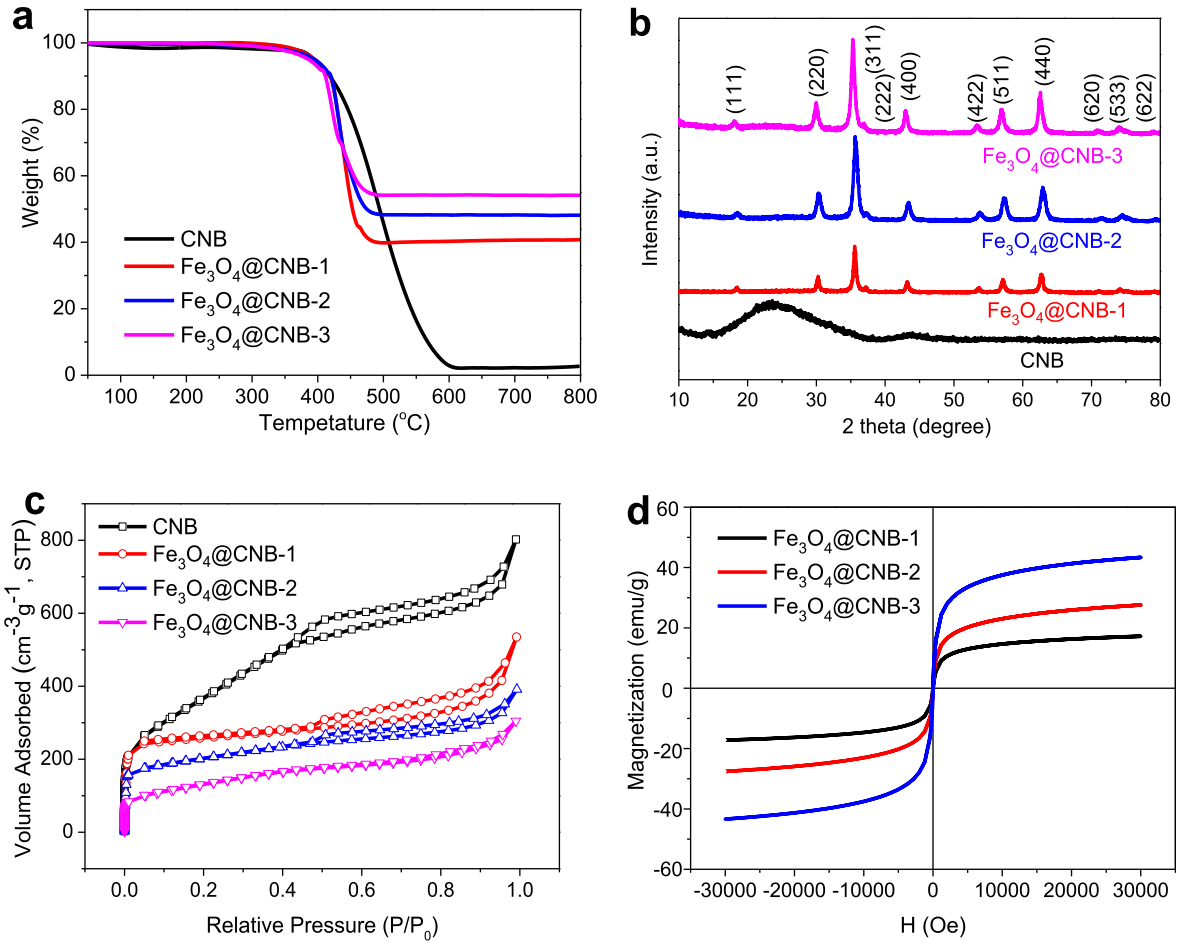

Fig. 2. (a) The thermogravimetric analysis (TGA) curves, (b) the XRD patterns of CNB, Fe_3O_4@CNB-1, Fe_3O_4@CNB-2 and Fe_3O_4@CNB-3 samples, (c) the Nitrogen adsorption–desorption isotherms, (d) the magnetic hysteresis curves for Fe_3O_4-carbon hybrid materials of CNB, Fe3O4@CNB-1, Fe3O4@CNB-2 and Fe3O4@CNB-3 samples. (A colour version of this figure can be viewed online.)

diffraction (XRD). Fig. 2b displays XRD spectra of pure CNB and Fe_3O_4@CNB composites. For CNB, the two typical broad peaks at 24.4°and 44° are from the (002) and (001) crystal planes of carbon (JCPDS 75–1621) [30]. For Fe_3O_4@CNBs, the diffraction peaks at 18.5°, 30.2°, 35.7°, 37.3°, 43.4°, 53.5°, 56.8°, 62.9°, 71°, 74.3° and 78.7° of Fe_3O_4@CNB composites can be indexed as (111), (220),

(311), (222), (400), (422), (511), (440), (620), (533) and (622) planes of face-centered cubic magnetite Fe_3O_4 (JCPDS 19–0629) [31]. It indicates that the precursor $Fe(NO_3)_3 \cdot 9H_2O$ is converted to Fe_3O_4 with no byproducts after the annealing process. In addition, two peaks appeared in Raman spectroscopy (Fig. S4a) of Fe_3O_4@CNB-2 at about 270 cm^{-1} and 671 cm^{-1} are associated with E_g and A_{1g} modes of Fe_3O_4. Combined with the TEM results, it can be confirmed that Fe_3O_4 nanoparticles were formed in the hollow cavity of CNB. The typical D and G modes at 1357 and 1594 cm^{-1} are present in both CNB and Fe_3O_4@CNB, corresponding to the defective carbon and sp2 graphitic carbon, respectively.

Fig. 2c illustrates the nitrogen (N_2) adsorption/desorption isotherms for pure CNB, Fe_3O_4@CNB-1, Fe_3O_4@CNB-2, and Fe_3O_4@CNB-3 samples, and the corresponding pore size distribution curves are shown Fig. S4b. Type IV isotherms with H4-type hysteresis loops were observed, indicating the presence of micropores, mesopores and macropores in the materials. The specific surface area of CNB, Fe_3O_4@CNB-1, Fe_3O_4@CNB-2, and Fe_3O_4@CNB-3 is 1400, 527, 467 and 374 $m^2\ g^{-1}$ (Table S1). The total volumes of pores in the samples are 0.92, 0.45, 0.42 and 0.41 $cm^3\ g^{-1}$, respectively. Not surprisingly, the surface area and pore volume were sharply reduced after Fe_3O_4 was incorporated into CNB [32]. The corresponding NLDFT pore size distribution curves demonstrate a similar pore size distribution from 0.56 to 30 nm, indicating the co-existence of micropores/mesopores in the samples. Since most Fe_3O_4 nanoparticles are larger than 20 nm (Seen from the TEM images) and located inside the hollow cavity of CNB, the introduction of Fe_3O_4 nanoparticles will neither block the pores nor greatly change the pore size distribution of CNB.

The magnetic saturation of magnetic materials can be studied through the hysteresis loop at room temperature. The magnetic hysteresis curves of Fe_3O_4-carbon hybrid materials under ±30 kOe magnetic field are shown in Fig. 2d. All Fe_3O_4-carbon hybrid materials have no obvious magnetic hysteresis and show good superparamagneticity. As the amount of Fe_3O_4 in Fe_3O_4-carbon hybrid materials gradually increases, the magnetic saturation (M_s) increases correspondingly. The observed magnetic saturation of Fe_3O_4@CNB-1, Fe_3O_4@CNB-2 and Fe_3O_4@CNB-3 are 17.2 emu g^{-1}, 27.6 emu g^{-1} and 43.3 emu g^{-1}, respectively, which are lower than the theoretical value of bulk Fe_3O_4 (92 emu g^{-1}). Nevertheless, it still indicates that the prepared Fe_3O_4-carbon hybrid composites have good magnetic properties.

Magnetic nanoparticles can benefit from the action of the magnetic field to obtain a response, which can induce not only surface electrostatic doping (electric double layer capacitance) but also interfacial redox reactions (Faraday pseudocapacitance) [33,34]. When the magnetic capacitor is in a charged state, electrons accumulate at the Fe_3O_4/electrolyte interface. This may change the local electronic structure of Fe_3O_4 and cause some Fe^{3+} to transform into Fe^{2+}, which leads to an increase in the net magnetic moment [35]. On the contrary, when Fe^{2+} is converted to Fe^{3+}, the saturation magnetization in the discharge decreases. The capacitance enhancement of the magnetic field on the Fe_2O_3-graphene hybrid can be doubled under an external 0.072 T magnetic field [36].

The Fe_3O_4@CNB samples were examined by X-ray photoelectron spectroscopy (XPS) to obtain the elemental composition and valence state information. The XPS spectrum of Fe_3O_4@CNB confirmed the presence of Fe, O, N and C elements in the samples (Fig. 3a). The high resolution N 1s, O 1s and Fe 2p XPS spectra peaks confirmed the successful doping of N and O in the Fe_3O_4@CNB (Fig. 3b–d). And the survey spectrum also gives the contents of C (71.2 at%), N (4.4 at%), O (16.82 at%) and Fe (7.52 at%) (Table S2). Based on the high-purity carbon of CNB, it can be calculated that the content of Fe_3O_4 in Fe3O4@CNB-2 is 52 wt%. The high N doping can be attributed to the introduced EDA into reaction system, which was used as both a base catalyst and nitrogen precursor, to achieve in-situ N doping in CNB during annealing treatment. The high oxygen content is originated from monomer resorcinol. In detail, the spectrum of N1s can be fitted into three dominant peaks at 398.3 eV, 400.4 eV, 401.2 eV, corresponding to pyridinic N, pyrrolic N, graphitic N, respectively. Pyridinic N and pyrrolic N can enhance electrical conductivity and provide partial pseudo-capacitance, and graphitic N can favorably promote electron transfer in electrode materials [37]. In the O 1s spectra, a large Fe–O peak was observed at 530.1 eV and peaks due to C–O and C–O–C were observed at 531.4 and 533.1 eV, respectively [38]. Fe 2p spectra show the peaks at 710.8 and 724.9 eV, which is assigned to Fe $2p_{3/2}$ and Fe $2p_{1/2}$ spin-orbit peaks, further demonstrating the existence of Fe_3O_4 nanoparticles in the composites [39]. Since CNB was first obtained at 900 °C, higher than the heat-treatment temperature at 400 °C for the subsequent thermal decomposition of $Fe(NO_3)_3 \cdot 9H_2O$ to obtain Fe_3O_4, there should be no direct formation of Fe–C bond in the composite material. The peaks at 711.1 and 713.6 eV in the Fe $2p_{3/2}$ region were attributed to Fe^{2+} and Fe^{3+}, and are related to the peaks at 724.4 and 726.9 eV in the Fe $2p_{1/2}$ region [40]. In addition, the peaks observed at 718.6 and 732.7 eV are the satellite peaks of Fe^{2+} and Fe^{3+}, respectively [41].

The as-prepared Fe_3O_4-carbon hybrid materials with well-dispersed Fe_3O_4 nanoparticles inside the cavity of CNB, developed porous structures and proper pore size distributions are expected to exhibit superior electrochemical performance as electrode materials for supercapacitors. Cyclic voltammetry (CV) and Galvanostatic Charge/Discharge (GCD) were performed in a conventional three-electrode configuration using 6 mol L^{-1} KOH solution as the electrolyte. Fig. 4a shows the CV curve of CNB and Fe_3O_4@CNB with different Fe_3O_4 contents (scan rate of 5 mV s^{-1}). These CV curves of CNB show a rectangular shape, indicating that the electric double layer capacitor (EDLC) is dominant with weak Faraday pseudocapacitance generated by N-doping and O-doping. Heteroatom doping (oxygen and nitrogen) may trigger redox reactions with changing electronic states at the doping sites or adjacent carbon atoms [42]. On the other hand, the Fe_3O_4@CNB composites exhibit a distorted rectangular shape and the integrated areas of curves are larger than pure C, which are due to the co-existence of EDLC and pseudocapacitance contributed from Fe_3O_4 and CNB. The pseudocapacitive characteristics of Fe_3O_4 originate from the redox reaction between Fe^{2+} and Fe^{3+} in KOH electrolyte [43].

The CV curves of samples at different scanning rates were displayed in Fig. 4b and Fig. S5 (from 5 to 200 mV s^{-1}). With the scanning rate going higher, the current response increases correspondingly. Even at a very high scan rate of 200 mV s^{-1}, the CV curves could also maintain a nearly-rectangular shape, because of the simultaneous occurrence of faradaic and non-faradaic processes to store energy [44]. As the scan rate increases, the deviation from the rectangularity of the CV curves becomes obvious, indicating that the effective interaction between the ions and the electrode is greatly reduced. In general, the CV curves of Fe_3O_4@CNB samples are almost rectangular, indicating the main double-layer capacitor properties during charging and discharging and the contribution of pseudo-capacitance to the total capacitance [45].

Total charge storage in an electrode consists of the non-faradaic contribution from the double-layer capacitance and faradaic contributions from charge transfer processes (referred to as pseudocapacitance) [46]. The contribution of faradaic behaviour to energy storage can be quantified based on the power-law relationship by separating the current (i) into capacitive effects(k_1v) and faradaic behaviour ($k_2v^{1/2}$) according to Ref. [47]:

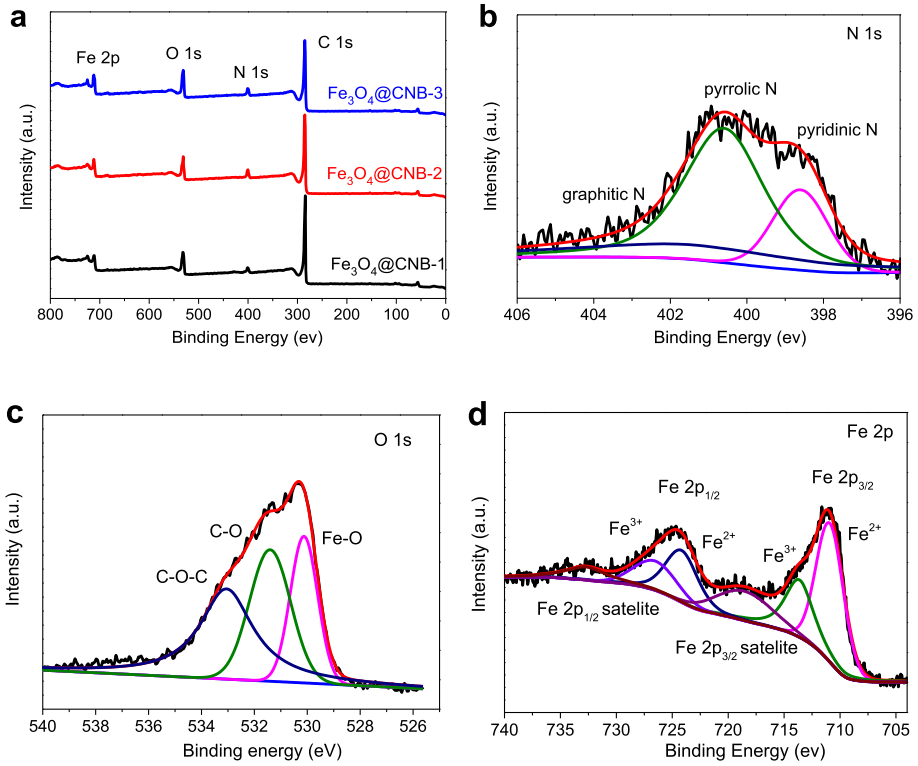

Fig. 3. (a) The X-ray photoelectron spectroscopy (XPS) survey spectrum, and high-resolution spectra of (b) N1s, (c) O 1s and (d) Fe 2p from Fe_3O_4@CNB-2. (A colour version of this figure can be viewed online.)

$$i = k_1 v + k_2 v^{1/2} \quad (1)$$

where v is the sweep rate, k_1 and k_2 are constants (Fig. 4c). As shown in Fig. 4d, the Fe_3O_4@CNB-2 have about 69% pseudocapacitance contribution by the redox at a scan rate of 5 mV s^{-1}. The pseudocapacitance contribution gradually decreases with an increase in scan rates and drops to 26% at 200 mV s^{-1}. This means that the kinetics of redox is slower than the scan rate [48].

The GCD curves of CNB and Fe_3O_4@CNB composites with different Fe_3O_4 contents are shown in Fig. 4e. All GCD curves are approximately isosceles triangular with no significant IR drop, indicating reversible supercapacitor behaviour and superior Coulomb efficiency. The gravimetric capacitances (C_g) of pure CNB, Fe_3O_4@CNB-1, Fe_3O_4@CNB-2, and Fe_3O_4@CNB-3 electrodes are calculated from GCD curves at different current densities from 1 A g^{-1} to 10 A g^{-1} (Fig. S6) by the following formula,

$$C_g = I\Delta t / m\Delta V \quad (2)$$

where I is the current density, Δt is the time of the discharge process, m is the mass of active materials, and ΔV is the electrical potential range. Compared with pure CNB (only 242 F g^{-1}), the introduction of Fe_3O_4 Nanoparticles enables the increasing of C_g of Fe_3O_4@CNB-1, Fe_3O_4@CNB-2, and Fe_3O_4@CNB-3 to 334, 466 and 387 F g^{-1}, respectively. All Fe_3O_4@CNB composites have higher C_g than pure CNB, showing the combined contribution of the EDLC of CNB and the pseudocapacitance of Fe_3O_4. Notably, the maximum C_g of 466 F g^{-1} achieved for the Fe_3O_4@CNB-2 samples was higher than Fe_3O_4@CNB-3 where the Fe_3O_4 nanoparticles filled the hollow interior of the CNB. The inherent problem of pure Fe_3O_4 as an electrode material is that only a very thin surface layer participates in the charge-discharge mechanism, while the Fe_3O_4 bulk core is difficult to induce faradaic reaction because of its low conductivity [49]. Specifically, the large amount of Fe_3O_4 nanoparticles is aggregated in Fe_3O_4@CNB-3, resulting in a lower electrical conductivity and reducing the effective utilization of the active component, which negatively affects the electrochemical performance. On the other hand, even at the highest current density (10 A g^{-1}), Fe_3O_4@CNB-2 still shows a high gravimetric capacitance of 341 F g^{-1} with the capacitance retention of 73.2% (Fig. 4f) due to both carbon-encapsulation and good utilization of Faradaic reaction of Fe_3O_4 nanoparticles. Therefore, Fe_3O_4 @ CNB-2 with a proper amount of Fe_3O_4 nanoparticles is more suitable to obtain better electrode materials for supercapacitors.

Volumetric capacitance (C_v) is also an important parameter for supercapacitor devices, especially when used in micro and portable electronic systems [50]. The bowl-shaped CNB structures formed due to the collapse of hollow spheres have a higher packing density as the particles are better stacked. The packing densities (ρ) were evaluated by the previously reported method (Fig. S7) [51]. By vacuum incipient wetness method, Fe_3O_4 nanoparticles are perfectly grown inside the CNB without changing the original bowl-shaped structure of CNB, which can increase the packing density of electrode materials (Table S1). Based on the GCD results, C_v can be obtained by the equation of $C_v = C_g \times \rho$. As shown in Fig. 5a, Fe_3O_4@CNB-2 has the largest volume specific capacitance (624 F cm^{-3}), which is more than twice that of CNB (247 F cm^{-3}). Compared with other electrode materials for supercapacitor (Fig. 5b and Table. S3), the unique bowl-like structure of Fe_3O_4@CNB and the appropriate loading of Fe_3O_4 nanoparticles give it superior gravimetric capacitance C_g and volumetric capacitance C_v simultaneously under similar current densities [52–58].

The electrochemical impedance spectroscopy (EIS) was used to study the capacitance resistance and charge transfer kinetics of electrode materials. All the Nyquist plots of the prepared electrode materials in Fig. 6a are composed of two parts: a small semicircle at

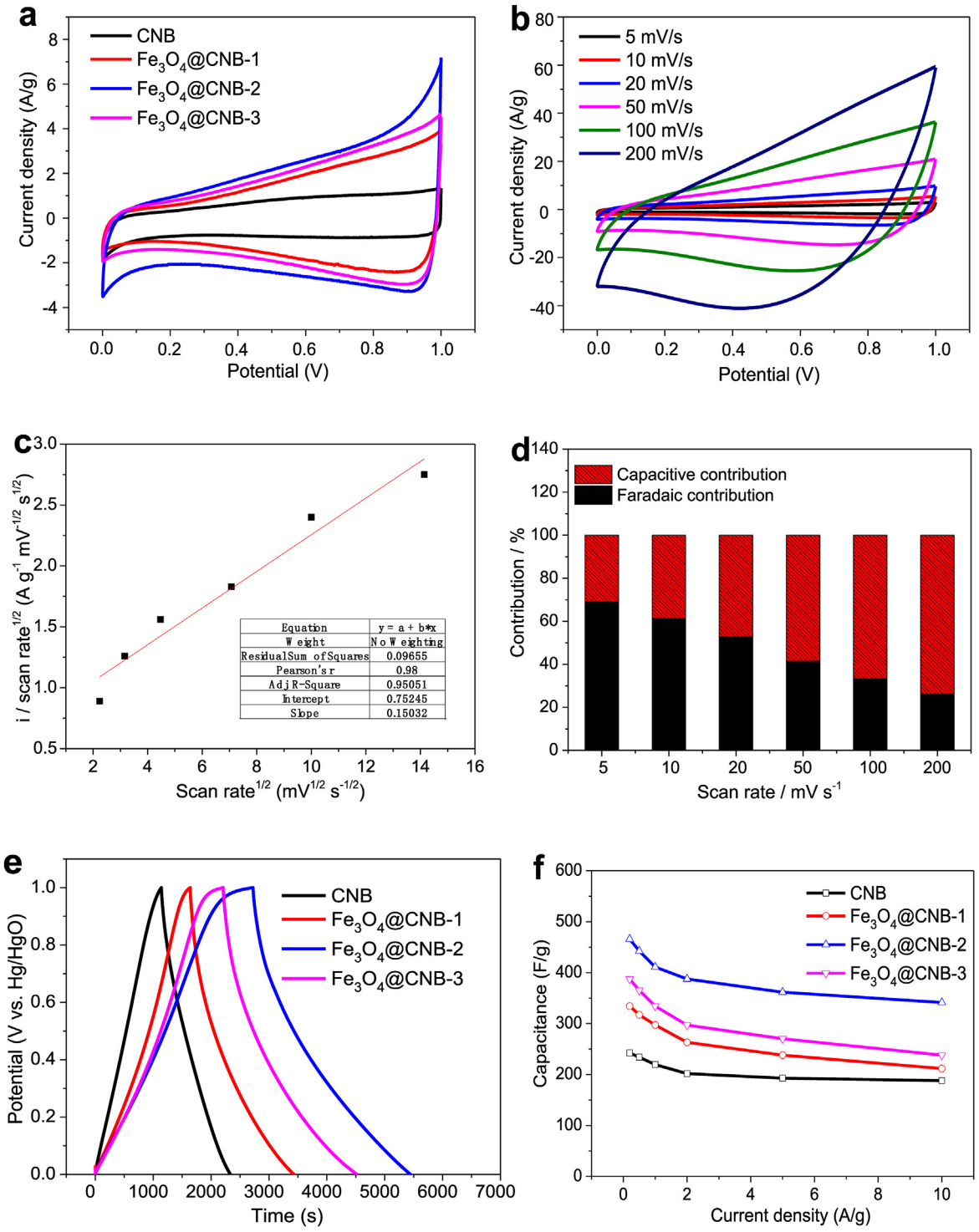

Fig. 4. (a) The Cyclic Voltammetry (CV) curves tested at 5 mV s^{-1} for all samples, (b) CV curves at the various scan rates for Fe_3O_4@CNB-2, (c) The determination of the k_1 and k_2 at 1.0 V for Fe_3O_4@CNB-2, (d) Contribution ratios of capacitances from the capacitive behavior and faradaic (redox) behavior at various scan rates for Fe_3O_4@CNB-2, (e) The Galvanostatic charge-discharge (GCD) curves measured at 0.2 A g^{-1} for all samples, and (f) corresponding gravimetric capacitance versus discharge current density from 0.2 A g^{-1} to 10 A g^{-1}. (A colour version of this figure can be viewed online.)

high frequency along with an inclined line at the low frequency corresponding to a diffusion process of the electroactive species. The inclined lines at low frequency deviate more from the Y-axis with the increasing content of Fe_3O_4, indicating that more Fe_3O_4 nanoparticles filled in CNB are not conducive to the diffusion of electroactive species and the adsorption onto the electrode surface of ion. Notably, the charge transfer resistance (R_{ct}) of CNB, Fe_3O_4@CNB-1, Fe_3O_4@CNB-2, and Fe_3O_4@CNB-3 are 0.68, 0.75, 0.78, and 2.21 Ω, respectively, which is explained by the gradual increase of Fe_3O_4 with low conductivity. Combined with TEM results in Fig. 1e–h, it is deduced that an appropriate amount of Fe_3O_4 nanoparticles filled inside the CNB can have good contact with the

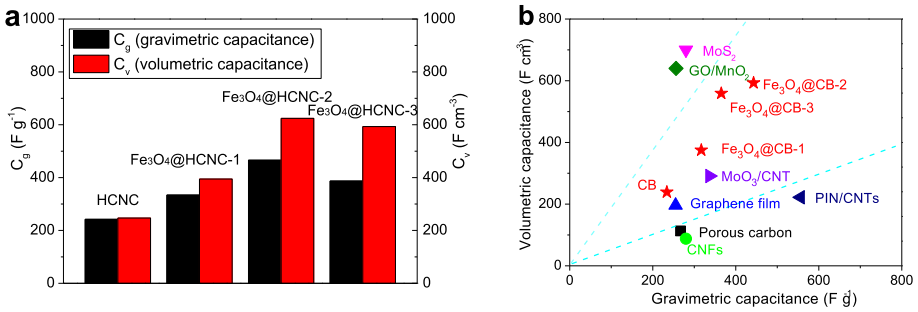

Fig. 5. (a) The volumetric capacitances vs gravimetric capacitances of Fe_3O_4-carbon hybrid materials at 0.2 A g^{-1}, and (b) C_v vs. C_g of the as-prepared electrode materials with previously reported related materials at 0.5 A g^{-1}. (A colour version of this figure can be viewed online.)

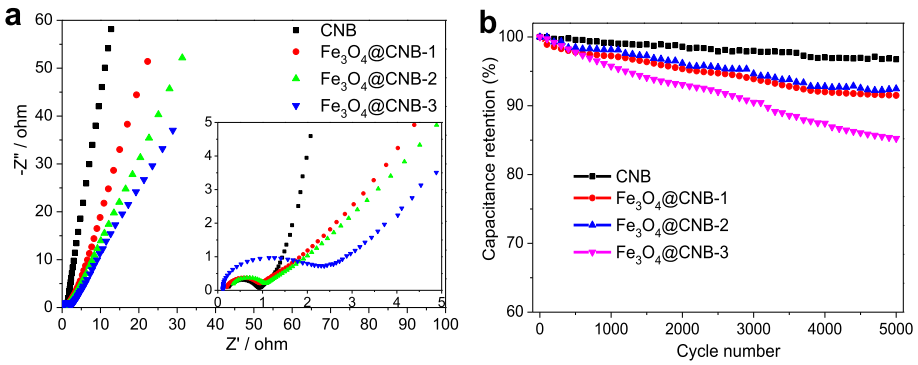

Fig. 6. (a) The Nyquist plot (the inset is the enlarged spectrum in the low impedance regime), and (b) cycling performance at 5.0 A g^{-1} for 5000 cycles. (A colour version of this figure can be viewed online.)

inner wall of the CNB, but too many Fe_3O_4 nanoparticles filled inside CNB such as that for Fe_3O_4@CNB-3, may exert significant ion transmission limitations. The cycling stability of the samples was obtained by performing the charge/discharge tests repetitively at a current density of 5.0 A g^{-1}. As shown in Fig. 6b, both CNB and Fe_3O_4@CNB composites have excellent capacitance retention even after 5000 cycles, demonstrating the long-term cycling stability of the materials. Therefore, it is evident that bowl-shaped hollow porous carbon nanocapsules with high pore volume and large hollow interior void can act as a buffer, which can relax the volumetric and structural changes caused by the Fe_3O_4 during the charge-discharge processes [59].

4. Conclusions

In summary, a new nanoscale architecture of Fe_3O_4-carbon hybrid materials prepared by a vacuum incipient wetness process was successfully developed and used for supercapacitor devices. The amount of Fe_3O_4 nanoparticles were controllably confined inside the cavity of the bowl-shaped hollow porous carbon nanocapsules (CNB). The bowl-shaped CNB possess a large surface area, hierarchical porosity, conductive carbon shell, high nitrogen (N) and oxygen (O) elemental doping and a hollow interior, which can not only provide stable electric double layer capacitance, but also serve as an excellent protective container for storing active materials. Fe_3O_4 nanoparticles are uniformly distributed in the hollow interior of CNB, which overcomes the deficiency of lower electrical conductivity and lower utilization of Fe_3O_4 for electrode material during the process of charging and discharging. Furthermore, the unique encapsulation of the Fe_3O_4 nanoparticles by the bowl-shaped CNB not only maintains the structural stability, shortens the pathway of electrolyte ions diffusion, but also enhances the volumetric capacitance of Fe_3O_4-carbon hybrid materials. Results of electrochemical tests reveal that when the Fe_3O_4@CNB with the appropriate amount of Fe_3O_4 were used as electrode materials, the supercapacitor devices can exhibit higher gravimetric capacitance C_g (466 F g^{-1}) and volumetric capacitance C_v (624 F cm^{-3}), and enhanced cyclic stability. This work provides a promising strategy for the preparation of hollow carbon nanocapsules loaded with metal oxide nanoparticles, and can also be easily extended to other metal sulfides/oxide-carbon hybrid materials structures for various emerging applications in the future.

CRediT authorship contribution statement

Lijian Wang: Investigation, Data curation, Writing – original draft. **Fenghua Liu:** Investigation, Data curation, Writing – original draft. **Avishek Pal:** Investigation, Data curation, Writing – original draft. **Yuesheng Ning:** Investigation, Data curation, Writing – original draft. **Zan Wang:** Investigation, Data curation, Writing – original draft. **Binyuan Zhao:** Conceptualization, Supervision, Resources, Project administration, Writing – review & editing, Funding acquisition. **Robert Bradley:** Conceptualization, Supervision, Resources, Project administration, Writing – review & editing, Funding acquisition. **Weiping Wu:** Conceptualization, Supervision, Resources, Project administration, Writing – review & editing, Funding acquisition.

Declaration of competing interest

The authors declare that they have no known competing financial interests or personal relationships that could have appeared to influence the work reported in this paper.

Acknowledgements

This work is supported by the Innovate UK (Grant 104013), the Science and Technology Commission of Shanghai Municipality (STCSM) (Grant 17230732700), and the CAS Pioneer Hundred Talents Program. This work is also supported by a Joint Research Center of Materials for Rail Transit between the State Key Laboratory of Metal Matrix Composites, Shanghai Jiao Tong University and the Economic and Technological Development Zone, Ma'anshan (project No. 2018GJ012).

Appendix A. Supplementary data

Supplementary data to this article can be found online at https://doi.org/10.1016/j.carbon.2021.04.024.

References

[1] P. Simon, Y. Gogotsi, B. Dunn, Where do batteries end and supercapacitors begin? Science 343 (2014) 1210–1211.
[2] M. Winter, R.J. Brodd, What are batteries, fuel cells, and supercapacitors? Chem. Rev. 104 (2004) 4245–4269.
[3] B.E. Conway, Transition from supercapacitor to battery behavior in electrochemical energy-storage, J. Electrochem. Soc. 138 (1991) 1539–1548.
[4] N. Choudhary, C. Li, J. Moore, N. Nagaiah, L. Zhai, Y. Jung, et al., Asymmetric supercapacitor electrodes and devices, Adv. Mater. 29 (2017), 1605336.
[5] P. Simon, Y. Gogotsi, Materials for electrochemical capacitors, Nat. Mater. 7 (2008) 845–854.
[6] F.M. Wu, J.P. Gao, X.G. Zhai, M.H. Xie, Y. Sun, H.Y. Kang, et al., Hierarchical porous carbon microrods derived from albizia flowers for high performance supercapacitors, Carbon 147 (2019) 242–251.
[7] H.R. Peng, B. Yao, X.J. Wei, T.Y. Liu, T.Y. Kou, P. Xiao, et al., Pore and heteroatom engineered carbon foams for supercapacitors, Adv. Energy Mater. 9 (2019), 1803665.
[8] Y.L. Cheng, L. Huang, X. Xiao, B. Yao, L.Y. Yuan, T.Q. Li, et al., Flexible and cross-linked N-doped carbon nanofiber network for high performance freestanding supercapacitor electrode, Nanomater. Energy 15 (2015) 66–74.
[9] H. Jiang, C.Z. Li, T. Sun, J. Ma, A green and high energy density asymmetric supercapacitor based on ultrathin MnO_2 nanostructures and functional mesoporous carbon nanotube electrodes, Nanoscale 4 (2012) 807–812.
[10] B. Kirubasankar, V. Murugadoss, J. Lin, T. Ding, M.Y. Dong, H. Liu, et al., In situ grown nickel selenide on graphene nanohybrid electrodes for high energy density asymmetric supercapacitors, Nanoscale 10 (2018) 20414–20425.
[11] Y. Wang, Z.Q. Shi, Y. Huang, Y.F. Ma, C.Y. Wang, M.M. Chen, et al., Supercapacitor devices based on graphene materials, J. Phys. Chem. C 113 (2009) 13103–13107.
[12] C.G. Liu, Z.N. Yu, D. Neff, A. Zhamu, B.Z. Jang, Graphene-based supercapacitor with an ultrahigh energy density, Nano Lett. 10 (2010) 4863–4868.
[13] J. Yan, Q. Wang, T. Wei, Z.J. Fan, Recent advances in design and fabrication of electrochemical supercapacitors with high energy densities, Adv. Energy Mater. 4 (2014), 1300816.
[14] V. Augustyn, P. Simon, B. Dunn, Pseudocapacitive oxide materials for high-rate electrochemical energy storage, Energy Environ. Sci. 7 (2014) 1597–1614.
[15] B.E. Conway, V. Birss, J. Wojtowicz, The role and utilization of pseudocapacitance for energy storage by supercapacitors, J. Power Sources 66 (1997) 1–14.
[16] J. Chen, K.L. Huang, S.Q. Liu, Hydrothermal preparation of octadecahedron Fe_3O_4 thin film for use in an electrochemical supercapacitor, Electrochim. Acta 55 (2009) 1–5.
[17] X. Du, C.Y. Wang, M.M. Chen, Y. Jiao, J. Wang, Electrochemical performances of nanoparticle Fe_3O_4/activated carbon supercapacitor using KOH electrolyte solution, J. Phys. Chem. C 113 (2009) 2643–2646.
[18] Y.X. Zeng, M.H. Yu, Y. Meng, P.P. Fang, X.H. Lu, Y.X. Tong, Iron-based supercapacitor electrodes: advances and challenges, Adv. Energy Mater. 6 (2016), 1601053.
[19] K. Vijayamohanan, T.S. Balasubramanian, A.K. Shukla, Rechargeable alkaline iron electrodes, J. Power Sources 34 (1991) 269–285.
[20] W.H. Shi, J.X. Zhu, D.H. Sim, Y.Y. Tay, Z.Y. Lu, X.J. Zhang, et al., Achieving high specific charge capacitances in Fe_3O_4/reduced graphene oxide nanocomposites, J. Mater. Chem. 21 (2011) 3422–3427.
[21] Z.S. Wu, G.M. Zhou, L.C. Yin, W. Ren, F. Li, H.M. Cheng, Graphene/metal oxide composite electrode materials for energy storage, Nanomater. Energy 1 (2012) 107–131.
[22] S.J. Li, A. Pasc, V. Fierro, A. Celzard, Hollow carbon spheres, synthesis and applications - a review, J. Mater. Chem. 4 (2016) 12686–12713.
[23] M.H. Yu, W.T. Qiu, F.X. Wang, T. Zhai, P.P. Fang, X.H. Lu, et al., Three dimensional architectures: design, assembly and application in electrochemical capacitors, J. Mater. Chem. 3 (2015) 15792–15823.
[24] X.C. Li, L. Zhang, G.H. He, Fe_3O_4 doped double-shelled hollow carbon spheres with hierarchical pore network for durable high-performance supercapacitor, Carbon 99 (2016) 514–522.
[25] P.S. Yuan, Q.S. Wu, Y.P. Ding, H.Q. Wu, X.C. Yang, One-step synthesis of iron-oxide-loaded functionalized carbon spheres, Carbon 47 (2009) 2648–2654.
[26] Z.S. Li, J.H. Che, B.L. Li, W. Luo, Z.S. Liu, D.H. Li, Preparation of carbon nanospheres/Fe_3O_4 composites and their supercapacitor performances, J. Mater. Sci. Mater. Electron. 28 (2017) 17388–17396.
[27] L. Wang, F. Liu, Y. Ning, R. Bradley, C. Yang, K.-T. Yong, et al., Biocompatible mesoporous hollow carbon nanocapsules for high performance supercapacitors, Sci. Rep. 10 (2020), 4306–4306.
[28] F. Pei, T.H. An, J. Zang, X.J. Zhao, X.L. Fang, M.S. Zheng, et al., From hollow carbon spheres to N-doped hollow porous carbon bowls: rational design of hollow carbon host for Li-S batteries, Adv. Energy Mater. 6 (2016), 1502539.
[29] X.Z. Shi, S. Zhang, X.C. Chen, T. Tang, E. Mijowska, Effect of iron oxide impregnated in hollow carbon sphere assymmetric supercapacitors, J. Alloys Compd. 726 (2017) 466–473.
[30] X.C. Dong, H. Xu, X.W. Wang, Y.X. Huang, M.B. Chan-Park, H. Zhang, et al., 3D graphene-cobalt oxide electrode for high-performance supercapacitor and enzymeless glucose detection, ACS Nano 6 (2012) 3206–3213.
[31] J.M. Zhao, R. Luque, W.J. Qi, J.P. Lai, W.Y. Gao, M.R.H.S. Gilani, et al., Facile surfactant-free synthesis and characterization of Fe_3O_4@3-aminophenol-formaldehyde core-shell magnetic microspheres, J. Mater. Chem. 3 (2015) 519–524.
[32] E. Kang, Y.S. Jung, A.S. Cavanagh, G.H. Kim, S.M. George, A.C. Dillon, et al., Fe_3O_4 nanoparticles confined in mesocellular carbon foam for high performance anode materials for lithium-ion batteries, Adv. Funct. Mater. 21 (2011) 2430–2438.
[33] M. Bibes, A. Barthelemy, Multiferroics: towards a magnetoelectric memory, Nat. Mater. 7 (2008) 425–426.
[34] H.Y. Huang, C. Ge, Q.H. Zhang, C.X. Liu, J.Y. Du, J.K. Li, et al., Electrolyte-gated synaptic transistor with oxygen ions, Adv. Funct. Mater. 29 (2019), 1902702.
[35] T. Yamada, K. Morita, K. Kume, H. Yoshikawa, K. Awaga, The solid-state electrochemical reduction process of magnetite in Li batteries: in situ magnetic measurements toward electrochemical magnets, J. Mater. Chem. 2 (2014) 5183–5188.
[36] J.H. Zhu, M.J. Chen, H.L. Qu, Z.P. Luo, S.J. Wu, H.A. Colorado, et al., Magnetic field induced capacitance enhancement in graphene and magnetic graphene nanocomposites, Energy Environ. Sci. 6 (2013) 194–204.
[37] X.L. Fang, S.J. Liu, J. Zang, C.F. Xu, M.S. Zheng, Q.F. Dong, et al., Precisely controlled resorcinol-formaldehyde resin coating for fabricating core-shell, hollow, and yolk-shell carbon nanostructures, Nanoscale 5 (2013) 6908–6916.
[38] N.A. Zubir, C. Yacou, J. Motuzas, X.W. Zhang, J.C.D. da Costa, Structural and functional investigation of graphene oxide-Fe_3O_4 nanocomposites for the heterogeneous Fenton-like reaction, Sci. Rep. 4 (2014) 4594.
[39] I. Oh, M. Kim, J. Kim, Fe_3O_4/carbon coated silicon ternary hybrid composite as supercapacitor electrodes, Appl. Surf. Sci. 328 (2015) 222–228.
[40] K.V.M.K. Kireeti, G. Chandrakanth, M.M. Kadam, N. Jha, A sodium modified reduced graphene oxide-Fe_3O_4 nanocomposite for efficient lead(II) adsorption, RSC Adv. 6 (2016) 84825–84836.
[41] H.L. Wang, M. Li, B. Wang, M. Wang, I. Kurash, X.Z. Zhang, et al., Magnetic Fe_3O_4 nanoparticle catalyzed chemiluminescence for detection of nitric oxide in living cells, Anal. Bioanal. Chem. 408 (2016) 5479–5488.
[42] M. Yang, Z. Zhou, Recent breakthroughs in supercapacitors boosted by nitrogen-rich porous carbon materials, Adv. Sci. 4 (2017), 1600408.
[43] W.J. Meng, W. Chen, L. Zhao, Y. Huang, M.S. Zhu, Y. Huang, et al., Porous Fe_3O_4/carbon composite electrode material prepared from metal-organic framework template and effect of temperature on its capacitance, Nanomater. Energy 8 (2014) 133–140.
[44] N. Sinan, E. Unur, Fe_3O_4/carbon nanocomposite: investigation of capacitive & magnetic properties for supercapacitor applications, Mater. Chem. Phys. 183 (2016) 571–579.
[45] F.F. Cao, M.T. Zhao, Y.F. Yu, B. Chen, Y. Huang, J. Yang, et al., Synthesis of two-dimensional CoS1.097/nitrogen-doped carbon nanocomposites using metal-organic framework nanosheets as precursors for supercapacitor application, J. Am. Chem. Soc. 138 (2016) 6924–6927.
[46] T. Brezesinski, J. Wang, S.H. Tolbert, B. Dunn, Ordered mesoporous alpha-MoO_3 with iso-oriented nanocrystalline walls for thin-film pseudocapacitors, Nat. Mater. 9 (2010) 146–151.
[47] G.M. Kim, W.G. Lim, D. Kang, J.H. Park, H. Lee, J. Lee, et al., Transformation of carbon dioxide into carbon nanotubes for enhanced ion transport and energy storage, Nanoscale 12 (2020) 7822–7833.
[48] Y.K. Kim, J.H. Park, J.W. Lee, Facile nano-templated CO_2 conversion into highly interconnected hierarchical porous carbon for high-performance supercapacitor electrodes, Carbon 126 (2018) 215–224.
[49] H.L. Wang, H.J. Dai, Strongly coupled inorganic-nano-carbon hybrid materials for energy storage, Chem. Soc. Rev. 42 (2013) 3088–3113.
[50] M. Ghidiu, M.R. Lukatskaya, M.Q. Zhao, Y. Gogotsi, M.W. Barsoum, Conductive two-dimensional titanium carbide 'clay' with high volumetric capacitance, Nature 516 (2014) 78–U171.
[51] Y.J. Zhai, H.Z. Mao, P. Liu, X.C. Ren, L.Q. Xu, Y.T. Qian, Facile fabrication of hierarchical porous rose-like $NiCo_2O_4$ nanoflake/$MnCo_2O_4$ nanoparticle composites with enhanced electrochemical performance for energy storage, J. Mater. Chem. 3 (2015) 16142–16149.
[52] X.Y. Zheng, W. Lv, Y. Tao, J.J. Shao, C. Zhang, D.H. Liu, et al., Oriented and interlinked porous carbon nanosheets with an extraordinary capacitive

performance, Chem. Mater. 26 (2014) 6896–6903.
[53] W. Li, F. Zhang, Y.Q. Dou, Z.X. Wu, H.J. Liu, X.F. Qian, et al., A self-template strategy for the synthesis of mesoporous carbon nanofibers as advanced supercapacitor electrodes, Adv. Energy Mater. 1 (2011) 382–386.
[54] Z.B. Lei, L. Lu, X.S. Zhao, The electrocapacitive properties of graphene oxide reduced by urea, Energy Environ. Sci. 5 (4) (2012) 6391–6399.
[55] M. Acerce, D. Voiry, M. Chhowalla, Metallic 1T phase MoS_2 nanosheets as supercapacitor electrode materials, Nat. Nanotechnol. 10 (2015) 313–318.
[56] Z.J. Cai, Q. Zhang, X.Y. Song, Improved electrochemical performance of polyindole/carbon nanotubes composite as electrode material for supercapacitors, electron, Mater. Lett. 12 (2016) 830–840.
[57] X. Zhao, L.L. Zhang, S. Murali, M.D. Stoller, Q.H. Zhang, Y.W. Zhu, et al., Incorporation of manganese dioxide within ultraporous activated graphene for high-performance electrochemical capacitors, ACS Nano 6 (2012) 5404–5412.
[58] X. Zhao, L.L. Zhang, S. Murali, M.D. Stoller, Q.H. Zhang, Y.W. Zhu, et al., Incorporation of manganese dioxide within ultraporous activated graphene for high-performance electrochemical capacitors, ACS Nano 6 (2012) 5404–5412.
[59] J.Z. Chen, Q.Y. Chen, J.L. Xu, C.P. Wong, Hybridizing Fe_3O_4 nanocrystals with nitrogen-doped carbon nanowires for high-performance supercapacitors, RSC Adv. 7 (2017) 48039–48046.